Experimental validation of lookup table-based abstraction of motor control for equivalent-circuit electric vehicle simulations

Electrical Engineering (2026) 108:375
https://doi.org/10.1007/s00202-026-03724-9

ORIGINAL PAPER

Experimental validation of lookup table-based abstraction of motor control for equivalent-circuit electric vehicle simulations

Elia Grano[1] · Tomáš Lažek[2] · Massimiliana Carello[1] · Ivo Pazdera[2]

Received: 20 April 2026 / Accepted: 5 August 2026

Abstract

This paper is part of an effort to bridge the gap between energetic and equivalent-circuit motor models used in system-level electric-powertrain simulations, balancing model fidelity with computational efficiency. The goal is to investigate the use of lookup tables as tools to abstract low-level motor control into a numerical optimization problem requiring few input data and minimal specialized knowledge, thereby making high-fidelity equivalent-circuit models more suitable for early-stage system-level powertrain studies. The approach was experimentally validated on a 600-W induction motor. Results demonstrate that the control based on lookup tables achieves torque, flux, stator current, and efficiency levels comparable to a traditional field-oriented control scheme. While the two methods use different current trajectories, the overall performance metrics remain similar, confirming the effectiveness of lookup tables as a simulation tool for electric-powertrain development, control strategy evaluation, and early-stage electric vehicle system studies.

Keywords Electric drives · Electric motors · Electric mobility · Electric vehicles · Lookup tables · Field-oriented control

1 Introduction

The transition from conventional to electrified powertrains [1] is reshaping road-vehicle design, driven by stringent emissions regulations [2], evolving consumer expectations, and rapid progress in battery systems [3] and power electronics. Electric-drive architecture and its control strategy have become key determinants of vehicle performance, energy consumption, and packaging constraints, increasing the demand for modeling approaches that accurately represent electrical interactions among the energy storage system (ESS), inverter, and electric machine. In this context, the PerfECT Design Tool [4] was developed as a structured, multi-step vehicle design workflow that explicitly addresses performance, energetic flows, electrical interactions, and thermal dynamics. The PerfECT framework contains a dedicated "currents" level aimed at early-stage studies where architecture choices, ESS sizing, and supply voltage limitations must be evaluated without the cost of full controller- or pulse width modulation (PWM)-level simulation. This design-level module provides the electrical fidelity required for system-level trade-offs while remaining suitable for repeated simulations and rapid iteration.

The PerfECT "currents" level implements a hybrid electric drive description [5] that captures the dominant ESS–inverter–motor interactions using two complementary abstractions: one for motor control and one for inverter modeling. Low-level motor control is encapsulated in stator current lookup tables (LUTs) that map torque requests to $d-q$ stator current pairs, enabling higher-level modules of the inverter model to predict stator currents, phase voltages, and power flows without simulating low-level motor control. Complementing this, the inverter is represented by a phenomenological model [5] that enforces the essential ESS-to-motor constraints: an AC voltage limit tied to the available DC voltage to avoid the inverter's nonlinear mod-

Elia Grano and Tomáš Lažek contributed equally to this work

✉ Tomáš Lažek
tomas.lazek@vut.cz

Elia Grano
elia.grano@polito.it

Massimiliana Carello
massimiliana.carello@polito.it

Ivo Pazdera
pazderai@vut.cz

[1] Department of Mechanical and Aerospace Engineering, Politecnico di Torino, 10129 Torino, Italy

[2] Department of Power Electrical and Electronic Engineering, Brno University of Technology, 61600 Brno, Czech Republic

Published online: 21 August 2026

ulation region, and a torque-saturation routine that ensures commanded $d-q$ currents remain within ESS and inverter capabilities. The combined LUT–inverter formulation reproduces the electrical limits relevant for architecture selection and sizing while keeping computational burden low and preserving the ability to run large numbers of design iterations.

The scope of the present work is to address the evaluation gap of such system abstractions through a physical implementation. The main contributions and novelties of this paper are summarized as follows:

- **Experimental Validation:** We provide a comprehensive experimental validation of the LUT control abstraction concept in steady-state conditions on a physical 600-W induction motor test bench. This complements the purely simulation-based analysis initiated in [6] by evaluating the real-world accuracy and viability of the tool.
- **Focus on Magnet-Free Traction Alternatives:** We deliberately apply and validate the proposed methodology on an induction machine. This directly responds to the current automotive industry trend of reducing reliance on rare-earth permanent magnet synchronous motors (PMSM) to mitigate supply-chain risks, making advanced simulation tools for alternative traction drives highly relevant.
- **Modified LUT Formulation:** We introduce a modified lookup table generation algorithm that accepts an explicit stator flux reference as a direct input rather than a mere upper bound, aligning the simulation approach with actual industrial control parameters.
- **Integration into Control Loop:** We present a modified control scheme where precomputed optimization LUTs are successfully embedded directly into a donor field-oriented control (FOC) system to replace the standard current reference generation blocks.

While this work validates the LUT concept in steady-state conditions, the comprehensive investigation of dynamic transients is reserved for future research.

2 Related work

In today's challenging automotive industry landscape [7], simulation platforms provide a vital virtual environment to analyze complex interactions between powertrain components, allowing for the maximization of overall vehicle performance from the earliest stages of the design process. However, the inherent trade-off between model fidelity and computational efficiency remains a central challenge in Electric Vehicle (EV) powertrain modeling. While offering granular accuracy, high-fidelity models are often computationally intensive and require a vast amount of input data. Conversely, simpler models reduce simulation runtime but often lack the detail necessary for a comprehensive analysis of system dynamics [8, 9]. The various methodologies comprising the current state of the art in EV modeling can be viewed along this spectrum.

Energetic models, which commonly employ efficiency maps for the main powertrain subsystems, represent a foundational approach in system-level EV simulations. These models abstract away the intricate electrical dynamics of the motor and inverter, treating them as simplified power conversion systems. This simplification makes them computationally light and easy to implement, which is advantageous for estimating high-level performance metrics (such as vehicle torque and power demands) and for real-time powertrain control tasks [10–12]. However, computationally light, energetic models lack the granularity to capture detailed electrical interactions, cannot accurately reproduce the constraints that an insufficient DC voltage imposes on motor operation, and are unreliable when the supply voltage fluctuates [13, 14].

At the opposite end of the fidelity–efficiency spectrum lie high-fidelity equivalent-circuit models. These models can provide a highly detailed representation of electric drive operation, precisely describing electrical quantities of interest such as stator current and voltage components. Such models are used for in-depth analysis where the intricate nuances of the electrical system are of paramount importance [15–17]. The main limitations of equivalent-circuit models arise directly from their high level of complexity, which makes them impractical for certain applications, especially in the early stages of the design process. They require the explicit implementation of low-level motor control strategies—a task that demands significant expertise and adds to the model's complexity—and necessitate a large amount of input data, which may not be readily available at the initial design phases. From a computational perspective, these models are burdensome to run, making them unsuitable for rapid, early-stage design iterations where simulation speed is key.

The intermediate ground between these extremes has been comparatively less explored. Among the few approaches available, the use of torque-constant and voltage-constant models relies on an analogy with DC machines [8, 17]. While this formulation introduces a minimal level of electrical detail, its predictive capability is limited, resembling that of efficiency maps. These constants are tied to the nominal control strategy and cannot be reliably applied under variations in motor control, power supply, or within the boundary regions of the performance envelope where nonlinear effects become significant.

2.1 Previous work

To address the shortcomings of the modeling approaches identified in Sect. 2, a standardized procedure was developed to generate LUTs that directly map torque requests to $d-q$ stator current pairs. The approach formulates, for each possible operating point, a numerical optimization problem whose solution is the $d-q$ current pair that best satisfies the selected optimality criterion under the imposed operating conditions. This numerical interpretation of the motor control problem transforms the design effort into the straightforward task of supplying the equivalent-circuit parameters to the LUT generation routine. The resulting LUT-based methodology offers significant flexibility. It can be applied to both synchronous [18] and induction machines [6], which allows the choice of different optimization criteria, and its accuracy can be adapted to the level of detail available in the equivalent-circuit parameter set. For instance, in [6] the LUT generation procedure was extended to a detailed induction machine model incorporating frequency-dependent iron losses [17] and nonlinear magnetizing inductance [19] and was solved for two distinct optimization targets: maximum torque per ampere (MTPA) and minimum electromagnetic power loss (MEPL).

Beyond torque request, LUTs must also incorporate information about the available DC voltage. Since this parameter may vary due to design choices (e.g., battery architecture, cell chemistries, power-converter ratings) and operating conditions, the DC voltage cannot be used directly as an LUT input. Instead, stator flux represents a more suitable parameter. In the original formulation proposed in [18] and [6], stator flux was introduced as an upper bound. This choice enabled the LUT generator to select the optimal stator flux value for each operating condition without exceeding the imposed limit, thereby embedding the flux controller function within the LUT itself. While this formulation proved convenient in early-stage simulations—where the stator flux limit can be computed online with relatively simple algorithms [5]—it departs from the industrial standard of employing a fixed flux reference [15, 20, 21]. To align more closely with real-world practices, a modified algorithm was later presented in [22], in which the LUT generation procedure accepts a stator flux reference as an explicit input.

3 Case study

To validate the LUTs as a simulation tool to abstract low-level motor control in system-level vehicle simulations, a 600 W induction motor is used as a case study. To isolate the effect of LUTs from that of the entire electric drive model, the LUTs are introduced into a donor FOC scheme with stator flux orientation, replacing its original modules for $d-q$ current references generation. To fit such control scheme, stator flux is used as second LUT input instead of stator flux limit. The process of LUTs generation is illustrated in Sect. 3.1 and the control scheme is outlined in Sect. 3.2.

3.1 Lookup tables generation

A stator flux-oriented equivalent circuit in the $d-q$ reference frame has been selected to describe the behavior of the tested motor, featuring nonlinear magnetizing inductance and frequency-dependent iron losses. In this framework, the stator flux is aligned with the d-axis. Thus the q-axis component of the stator flux is zero. Although in practice estimation inaccuracies can introduce a marginal q-axis flux component, this idealized alignment is assumed for the formulation of the model. A schematic representation is shown in Fig. 1.

The motor parameters are provided in Tables 1 and 2.

The stator voltage components in the $d-q$ reference frame, $u_{s,d}$ and $u_{s,q}$, can be expressed as functions of the corresponding stator current components, $i_{s,d}$ and $i_{s,q}$, as shown in Eqs. 1 and 2:

$$u_{s,d} = R_s\, i_{s,d} + \dot{\Psi}_s, \tag{1}$$

$$u_{s,q} = R_s\, i_{s,q} + \omega_s\, \Psi_s. \tag{2}$$

where R_s represents the stator winding resistance, Ψ_s is the stator flux, and ω_s denotes the stator frequency. The definition of stator flux leads to Eq. 3:

$$\Psi_s = L_s\, i_\mu \tag{3}$$

here, L_s is the magnetizing inductance and i_μ is the magnetizing current. Under these conditions, only the q-axis rotor current component, $i_{r,q}$, contributes to the production of electromagnetic torque, which is expressed in Eq. 4:

$$T = \frac{3}{2}\, p\, \Psi_s\, i_{r,q} \tag{4}$$

where T is the developed torque and p is the number of pole pairs. The slip frequency, ω_{sl}, is obtained through Eq. 5, a more accurate expression than that used in previous works [6]:

$$\omega_{sl} = \frac{2\, R_r\, T}{3\, p\, \Psi_s^2} \tag{5}$$

with R_r denoting the rotor resistance. The stator frequency can be decomposed into the rotor mechanical frequency, ω_m, and the slip frequency, as given in Eq. 6:

$$\omega_s = p\, \omega_m + \omega_{sl} \tag{6}$$

Iron losses are represented through a parallel resistance, R_{Fe}, connected to the magnetizing inductance. The resulting iron

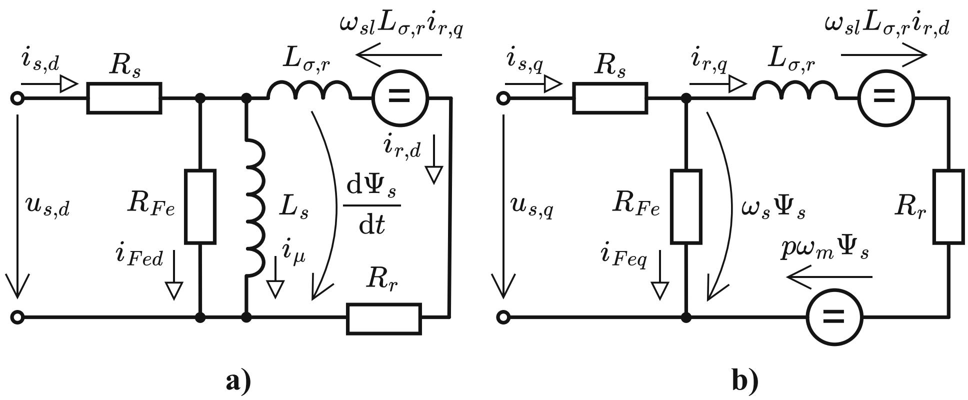

Fig. 1 **a** d-axis equivalent-circuit model; **b** q-axis equivalent-circuit model

Table 1 Nominal ratings and equivalent-circuit parameters of the tested induction machine (measured at 20 °C)

	Symbol	Value
Nominal ratings		
Nominal torque	T_n	2 Nm
Nominal speed	n_n	2850 rpm
Nominal frequency	ω_0	100π rad s^{-1}
Output power	P_{out}	600 W
Nominal voltage	u_s	230/400 V
Nominal current	i_n	1.4A
Efficiency	η	78.9 %
Pole-pairs	p	1
Equivalent-circuit parameters		
Stator resistance	R_s	11.74 Ω
Rotor resistance	R_r	8.70 Ω
Rotor leakage inductance	$L_{\sigma,r}$	0.1 H
Measured iron loss resistance at nominal frequency	R_{Fe0}	4300 Ω
Nominal stator flux	Ψ_n	0.9677 Vs

loss current is evaluated separately for the d-axis and q-axis components. In the d-axis, the iron loss current i_{Fed} is neglected because, under steady-state conditions, the voltage drop across R_{Fe} is essentially zero, yielding $i_{Fed} \approx 0$. Conversely, in the q-axis, the loss current is determined by the stator flux and synchronous frequency. Consequently, the active iron loss current is considered predominantly in the q-axis as $i_{Feq} = i_{Fe}$, expressed by Eq. 7:

$$i_{Fe} = i_{Feq} = \frac{\omega_s \, \Psi_s}{R_{Fe}} \tag{7}$$

In simplified models, R_{Fe} and L_s may be considered constant. However, to capture nonlinear effects, the iron loss resistance is modeled as frequency-dependent [17], and the magnetizing inductance is often expressed as a flux-dependent polynomial [19], as shown in Eqs. 8 and 9:

$$R_{Fe} = \frac{\omega_s}{\omega_{s0}} R_{Fe0} \tag{8}$$

$$L_s = \sum_{j=0}^{5} c_j \, \Psi_s^j \tag{9}$$

To enable the optimization, motor model equations are rewritten as optimization expressions (oe), i.e., explicit functions of the optimization variable (ov), the q-axis stator current, $i_{s,q}^{ov}$. Assuming constant machine parameters, the relevant expressions are:

$$i_{r,q}^{oe} = i_{s,q}^{ov} - i_{Fe} \tag{10}$$

$$i_{r,d}^{oe} = \frac{\omega_{sl} \, L_{\sigma,r} \, i_{r,q}^{oe}}{R_r} \tag{11}$$

$$i_{s,d}^{oe} = i_{r,d}^{oe} + i_\mu \tag{12}$$

According to Eq. 4, the electromagnetic torque depends on the rotor current in the q-axis, which is considered as an optimization variable. Then:

Table 2 Parameters of the nonlinear magnetizing inductance model

Parameter	Symbol	Value
Zero order term	c_0	0.1728 H
First order term	c_1	$6.526\ \mathrm{H\,V^{-1}\,s^{-1}}$
Second order term	c_2	$-15.67\ \mathrm{H\,V^{-2}\,s^{-2}}$
Third order term	c_3	$17.71\ \mathrm{H\,V^{-3}\,s^{-3}}$
Fourth order term	c_4	$-9.696\ \mathrm{H\,V^{-4}\,s^{-4}}$
Fifth order term	c_5	$1.841\ \mathrm{H\,V^{-5}\,s^{-5}}$

$$T^{oc} = \frac{3}{2}\, p\, \Psi_s\, i_{r,q}^{oe} \tag{13}$$

In addition to the constraints imposing the motor operating conditions—rotor speed, stator flux and torque—other conditions may be introduced, for example to impose a maximum stator current amplitude like in Eq. 14:

$$i_{s,\max}^{oc} \leq \sqrt{\left(i_{s,d}^{oe}\right)^2 + \left(i_{s,q}^{ov}\right)^2} \tag{14}$$

Finally, an optimality criterion must be specified. Here the MEPL strategy is adopted, which aims at minimizing electromagnetic losses. These are the summation of copper losses at the stator winding, copper losses at the rotor winding and iron losses. Therefore, the objective function can be expressed as shown in Eq. 15:

$$J = R_s\left((i_{s,d}^{oe})^2 + (i_{s,q}^{ov})^2\right) + R_r\left((i_{r,d}^{oe})^2 + (i_{r,q}^{oe})^2\right) \\ + R_{Fe}\, i_{Fe}^2 \tag{15}$$

The way the expressions outlined in this section are arranged together in an algorithm to generate the LUTs is schematized in the pseudocode in Fig. 2.

3.2 Motor control scheme

The original motor control scheme is shown in Fig. 3. The control strategy decouples torque and flux control by aligning the d-axis of the rotating reference frame with the stator flux vector Ψ_s. The outer speed control loop compares the reference speed ω_{ref} with the measured rotor speed ω (from the encoder) to generate the reference torque-producing current $i_{s,q,ref}$. The flux reference $\Psi_{s,ref}$ is used to compute the magnetizing current reference $i_{s,d,ref}$ through a flux-control proportional integral (PI) controller. The current control loop consists of two decoupled PI controllers, which regulate $i_{s,d}$ and $i_{s,q}$ and generate the corresponding voltage references $u_{s,d,ref}$ and $u_{s,q,ref}$ in the $d-q$ frame. These are transformed to $\alpha-\beta$ voltages and then to three-phase voltage references by means of space vector modulation (SVM).

The flux estimator provides the stator flux vector Ψ_s and slip angular frequency ω_{sl}, which, combined with the measured rotor speed, yield the reference frame angular velocity ω_s. This ensures correct orientation of the $d-q$ frame with respect to the stator flux.

In the modified motor control scheme, shown in Fig. 4, the reference generation stage of the FOC is augmented with the precomputed LUTs. These LUTs provide the d-and q-axis current references $i_{s,d,ref}$ and $i_{s,q,ref}$ as functions of the requested electromagnetic torque T_{ref} and stator flux Ψ_s (and other variables depending on the used equivalent-circuit model, like mechanical speed in this case).

In this configuration, the outer speed controller and the flux controller operate differently from the baseline FOC, producing T_{ref} and $\Psi_{s,ref}$ respectively. These signals are fed to the LUT block, which outputs $i_{s,d,ref}$ and $i_{s,q,ref}$ directly. The rest of the control structure, including the current controllers, voltage synthesis, and SVM, remains unchanged.

The modified control scheme is not intended to improve control performance with respect to the traditional FOC. Instead, its purpose is to validate the accuracy of the LUT-generated current references by comparing the resulting current trajectories and machine performance with those obtained by the FOC. To ensure a consistent baseline for comparison, the modified controller retains both the magnetic flux and speed control loops from the original control scheme. Therefore, the modified structure serves primarily to evaluate the LUTs on a physical drive and verify the accuracy of the generated current references. Importantly, this experimental validation focuses exclusively on steady-state accuracy and energy-efficiency mapping, while the investigation of dynamic transient behavior is reserved for future research.

4 Experimental results

This section presents the overall framework for the experimental testing of the discussed control strategies. First, Sect. 4.1 details the physical laboratory test bench, including the hardware configuration and measurement equipment. Subsequently, Sect. 4.2 provides the experimental results alongside a comprehensive discussion of the evaluated control performance. Finally, Sect. 4.3 addresses the practical considerations and system boundaries of the proposed LUT-based implementation.

4.1 Setup for experimental validation

A picture of the experimental setup is provided in Fig. 5, whereas Fig. 6 presents its schematic representation for

Fig. 2 Pseudocode for the LUTs generation algorithm

Define optimization variable: $i_{s,q}^{ov}$
for each ω_r in rotor frequency vector **do**
  for each Ψ_s in flux vector **do**
    for each T in torque request vector **do**
      Impose operating conditions through ω_r, Ψ_s and T:

$$L_s = \sum_{j=0}^{5} c_j \Psi_s^j \quad \text{(Eq. 9)}$$

$$i_\mu = \frac{\Psi_s}{L_s} \quad \text{(Eq. 3)}$$

$$\omega_{sl} = \frac{2\ R_r T}{3p{\Psi_s}^2} \quad \text{(Eq. 5)}$$

$$\omega_s = p\omega_m + \omega_{sl} \quad \text{(Eq. 6)}$$

$$R_{Fe} = \frac{\omega_s}{\omega_{s0}} R_{Fe0} \quad \text{(Eq. 8)}$$

$$i_{Fe} = \frac{\omega_s \Psi_s}{R_{Fe}} \quad \text{(Eq. 7)}$$

      Define optimization expressions:

$$i_{r,q}^{oe} = i_{s,q}^{ov} - i_{Fe} \quad \text{(Eq. 10)}$$

$$i_{r,d}^{oe} = \frac{\omega_{sl} L_{\sigma,r} i_{r,q}^{oe}}{R_r} \quad \text{(Eq. 11)}$$

$$i_{s,d}^{oe} = i_{r,d}^{oe} + i_\mu \quad \text{(Eq. 12)}$$

      Impose optimization constraints:

$$T^{oc} = \frac{3}{2} p\, \Psi_s i_{r,q}^{oe} \quad \text{(Eq. 13)}$$

$$\sqrt{\left(i_{s,d}^{oe}\right)^2 + \left(i_{s,q}^{ov}\right)^2} \le i_{s,max}^{oc} \quad \text{(Eq. 14)}$$

      Define objective function:

$$J = R_s\left((i_{s,d}^{oe})^2 + (i_{s,q}^{ov})^2\right) + R_r\left((i_{r,d}^{oe})^2 + (i_{r,q}^{oe})^2\right) + R_{Fe} i_{Fe}^2 \quad \text{(Eq. 15)}$$

      Solve optimization problem: min J subject to constraints
      if feasible solution found **then**
        Store ($i_{s,d}^{oe}, i_{s,q}^{ov}$) in LUT
      else
        Mark as non-compliant
      end if
    end for
  end for
end for

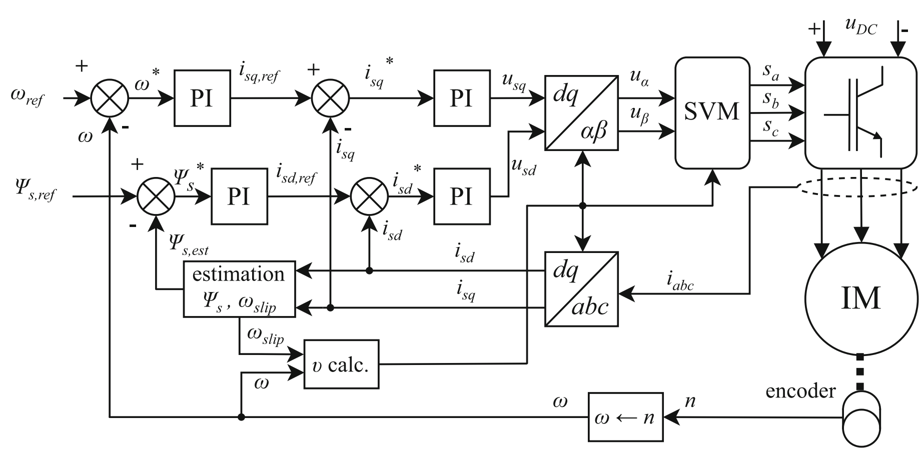

Fig. 3 FOC scheme

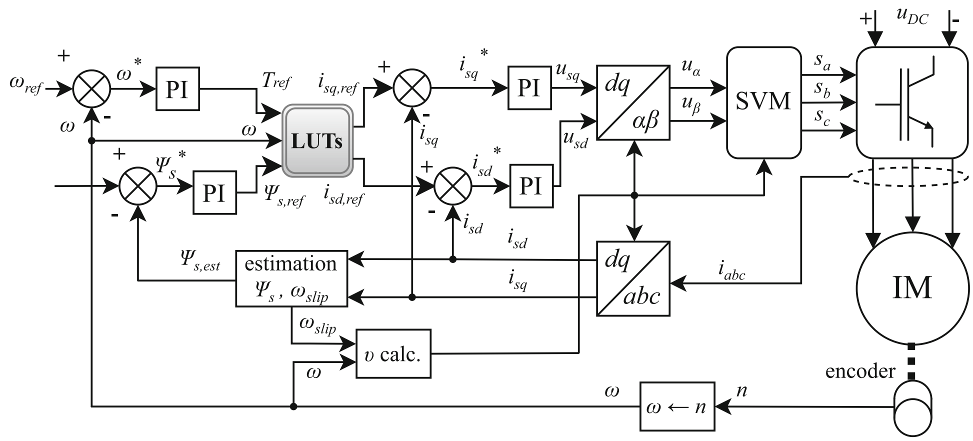

Fig. 4 LUTs-based control scheme

improved clarity. The physical assembly and measurement chain components are summarized in Table 3. The tested motor, denoted as EM1, is mechanically connected to a second motor, denoted as EM2, which serves as a dynamometer providing a controlled mechanical load. The inverter driving EM1 was supplied directly from a three-phase grid and was equipped with a braking resistor to dissipate regenerative energy and ensure DC bus stability during various load conditions.

The control algorithms were implemented on The entire "STM32G474RE" label of MCU did not wrap to the first column and extends into the second column (STMicroelectronics) 32-bit microcontroller featuring an ARM Cortex-M4 core and a floating-point unit. The control structure was developed using a model-based design (MBD) workflow within the Matlab/Simulink environment, utilizing the X2C tool [23] (Linz Center of Mechatronics) for automatic C-code generation. The block-oriented implementation within the X2C environment directly corresponds to the control scheme illustrated in Fig. 3 for FOC control scheme and Fig. 4 for proposed LUT-based control scheme. Both the LUT-based abstraction and the reference FOC were executed at a switching and sampling frequency of 10 kHz, ensuring deterministic real-time performance.

Data acquisition was performed using a dual-stream workflow to capture both internal and external variables. Internal control signals, including currents (i_{sd}, i_{sq}) and flux, were recorded directly from the microcontroller's RAM using the STM32CubeMonitor tool. Simultaneously, external parameters were captured through a National Instruments cDAQ-9188 chassis interfaced with LabVIEW custom graphical user interface (GUI). A ZES Zimmer LMG641 precision power analyzer was utilized for high-accuracy measurement of phase currents and voltages at the motor terminals. Shaft torque was acquired using a Magtrol TM309 transducer. To ensure a stable mean torque reading for steady-state validation, the analog torque signal was processed through a differential low-pass filter with a time constant 720 μs before being recorded by an NI 9222 card. Rotational speed was acquired using an external incremental encoder connected directly to the microcontroller for real-time control feedback. Winding and ambient temperatures were captured using a 24-bit NI 9219 module in a four-wire (Kelvin) configuration to eliminate lead resistance errors.

To ensure temporal alignment between the internal MCU data and the external NI-based measurements, a synchronization pulse was utilized to trigger both systems at the start of each test sequence. Finally, both datasets were exported in CSV format and processed in MATLAB to merge the data and generate the graphical results.

The baseline accuracies of the measurement instruments are detailed in Table 3. Due to the continuous thermal drift of the machine under load, the reported values are time-averaged over the respective acquisition windows. While rigorous statistical and repeatability analyses are common, they are omitted here. For this proof-of-concept study, the primary focus is on macroscopic control trends and energetic equivalence, which are clearly observable and significantly exceed the baseline sensor uncertainties.

4.2 Results and discussion

LUTs were generated using the steady-state equivalent-circuit model of the induction machine. To evaluate their performance, a stepped-torque test was designed to examine motor behavior under different load conditions. In each step, the mechanical torque was held constant for a sufficient duration to allow transients to settle, enabling a steady-state comparison between the LUT-controlled and FOC-controlled motor responses.

The stepped-torque profile was executed at constant speed and constant flux. To investigate the influence of operating conditions, three different speed levels and two different flux levels were tested. The speed level is indicated at the top of each diagram in the subsequent figures, with values set at 950 rpm, 1900 rpm, and 2850 rpm. The two flux levels are

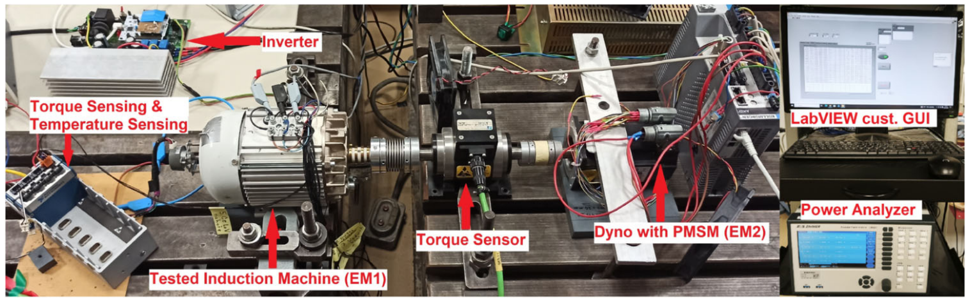

Fig. 5 Test setup

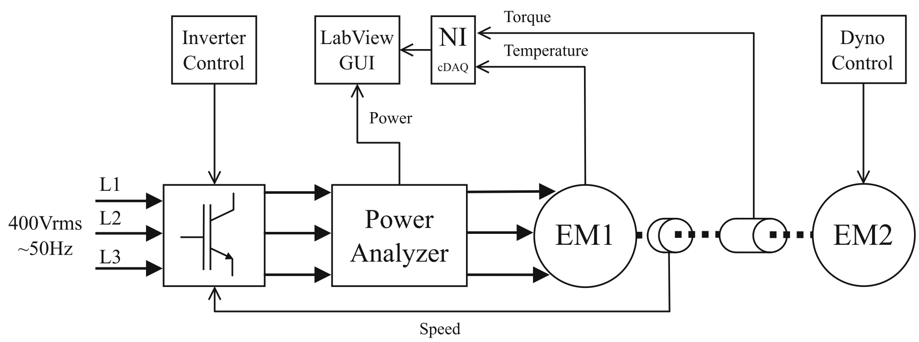

Fig. 6 Test setup schematics

Table 3 Specifications of the laboratory equipment utilized in the experimental validation

Device type	Manufacturer and model	Precision/key specifications
Power analyzer	ZES Zimmer LMG641	±0.015% of reading + ±0.01% of range*
DAQ chassis	NI CompactDAQ 9188	Ethernet-based, deterministic timing
Temperature module	NI 9219	24-bit, 4-wire RTD mode, ±0.1% gain error
Torque input card	NI 9222	16-bit, ±0.02% of reading + ±0.01% of range
Incremental encoder	Hengstler F14	4096 ppr, quadrature TTL interface
Torque sensor	Magtrol TM309	Rated torque (RT) 20 Nm, < ±0.1% of RT
Tested motor (EM1)	ATAS T22VT512	See Table 1
Dyno motor (EM2)	Kollmorgen AKM42E	PMSM servo: 3.32 Nm; 4000 rpm; 1.1 kW
Dyno drive (EM2)	Kollmorgen AKDP00307	Integrated speed/torque control loop

*Internal sensors was used

Table 4 Overview of evaluated operating cases for LUT-based control and traditional FOC

Case	LUT Control		Traditional FOC		Torque profile
	Speed (%)	Flux (%)	Speed (%)	Flux (%)	
1	100	100	100	100	Step profile (up to 100% T_n)
2	67	100	67	100	
3	33	100	33	100	
4	100	88	100	88	
5	67	88	67	88	
6	33	88	33	88	

All cases utilize a dynamic torque step profile up to 100% of the rated torque $T_n = 2.0$Nm. Rated base speed $n_n = 2850$ rpm, rated stator flux $\Psi_n = 0.9677$ Vs

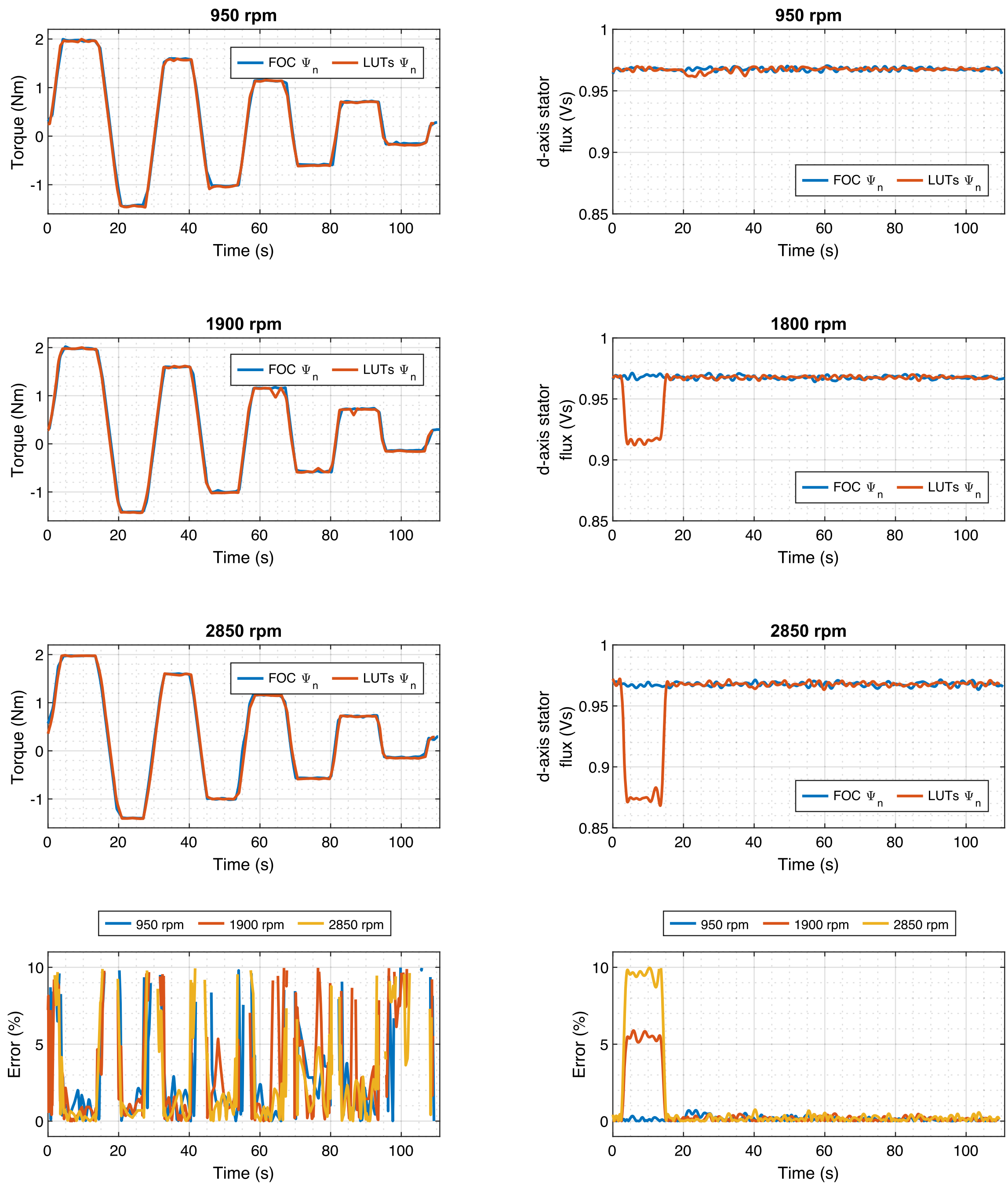

Fig. 7 Measured torque and flux profiles under nominal flux conditions

denoted in the legends as nominal flux Ψ_n (0.9677 Vs) and reduced flux Ψ_{rdc} (0.850 Vs). An overview of all evaluated operating cases relative to the rated motor specifications for both LUT-based control and traditional FOC is summarized in Table 4. To ensure a consistent thermal baseline across the experiments, all measurement sequences were initiated at a motor temperature of 40 °C, which was chosen to reflect an equivalent mean continuous load of the machine.

Figures 7 and 8 illustrate the tracking performance of the two control schemes under nominal and reduced flux conditions, respectively. Notably, the initial steady-state step in the 2850 rpm profile (bottom subplot in Fig. 7) was purposely chosen to explicitly demonstrate the motor operating at its rated operation point (2 Nm, 2850 rpm, and 0.9677 Vs). A good correlation between the torque profiles obtained with FOC and with LUT-based current reference generation is observed, with differences remaining below 3% for most

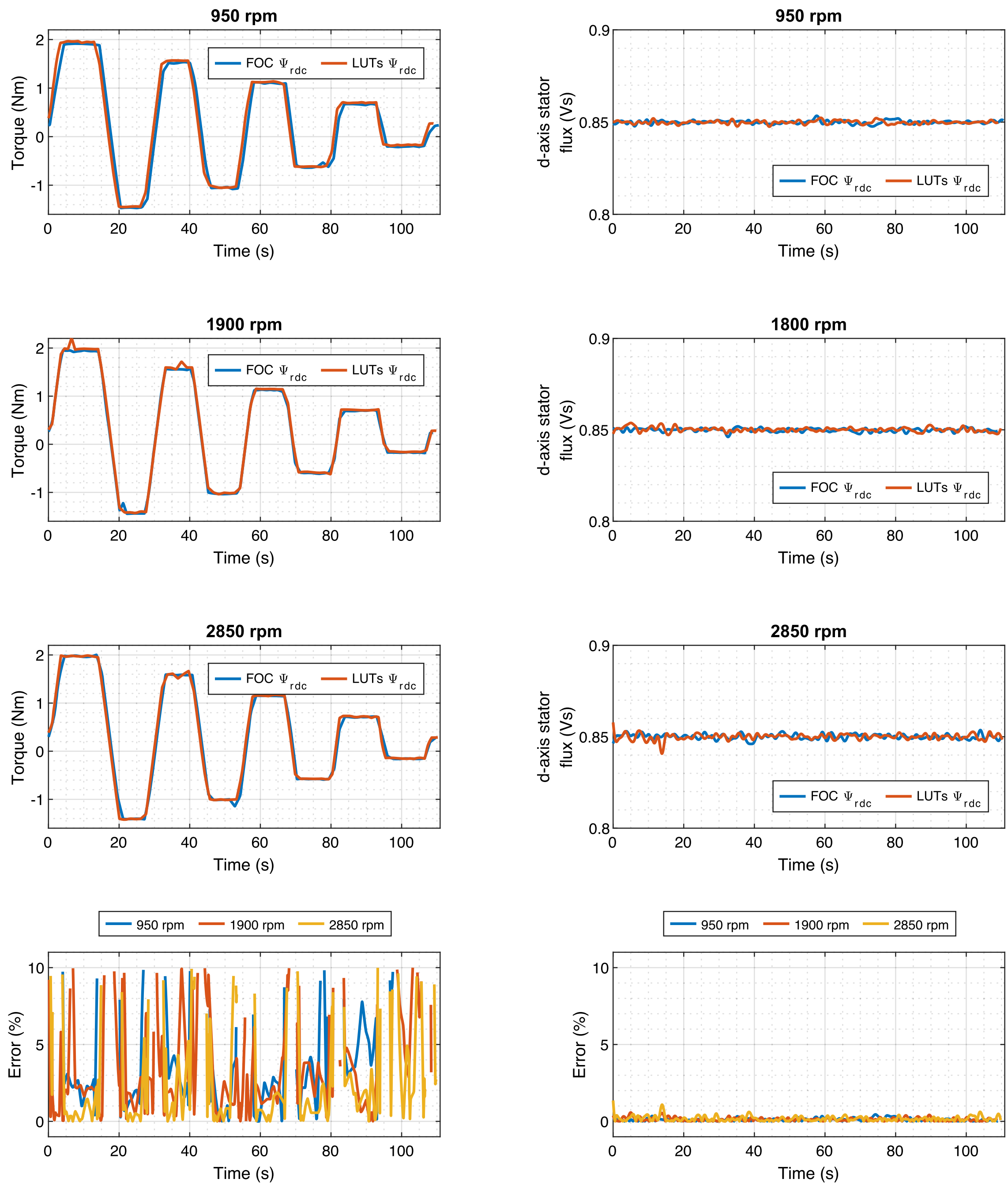

Fig. 8 Measured torque and flux profiles under reduced flux conditions

steady-state phases. The deviation is smallest under nominal flux and tends to increase with torque amplitude, which is likely due to the amplification effect that occurs when the percentage error is calculated with a smaller denominator.

It is worth emphasizing that torque is measured at the motor shaft; thus, the observed differences are not caused by poor tracking of the LUT-controlled scheme but result from the closed-loop nature of the control structure. Torque can be regarded as the control action exerted by the outer speed control loop, and its final value is influenced by the performance of the flux and current control loops.

In contrast to torque, deviations in the output flux are primarily attributable to the tracking performance of the flux-control loop. The flux error remains very small for most operating points, consistently below 1%. However, a notable deviation is observed at the 2 Nm torque step under nominal flux conditions, where the steady-state error reaches approximately 5% at 1900 rpm and increases to about 10% at 2850 rpm.

The observed flux drop under high loads stems from the lack of temperature compensation in the LUTs. As shown in Fig. 9, the outer flux controller attempts to compensate for thermal drifts by increasing the flux reference supplied to the LUT block. Nevertheless, when the requested flux reaches the LUT upper saturation boundary, set to 1.1 Vs, no further compensation is possible, and the commanded stator d-axis current becomes limited. At this saturated state, temperature-induced parameter variations take effect: the rapid temperature rise increases the rotor resistance, and the resulting higher slip frequency draws an elevated d-axis rotor current. Because the stator d-axis current is held constant by the LUT limit, this increased rotor current demand reduces the available magnetizing current (according to Eq. (12)), leading to a reduction in the actual stator flux. The influence of rotor speed further compounds this effect; at lower speeds, the q-axis rotor current is smaller, which reduces the internal voltage drops and mitigates the flux error. This saturation issue could theoretically be resolved by extending the maximum flux boundary defined in the LUTs or by incorporating temperature-dependent parameter adaptation. However, as detailed later in Sect. 4.3, introducing a thermal dimension conflicts with the primary objective of keeping the methodology computationally light for early-stage simulations.

Figures 10 and 11 show the d and q-axis stator current profiles under nominal and reduced flux conditions. These results highlight that LUT-based and FOC-based control achieve the same torque and flux targets through different current trajectories. This deviation arises directly from the differences in the underlying machine models: while standard FOC relies on a simplified linear representation that assumes constant magnetizing inductance and neglects iron losses, the LUTs are generated using a detailed model accounting for both nonlinear magnetic saturation and an equivalent iron loss resistance (R_{Fe}).

The q-axis current generated by the LUT-based control remains closer to the theoretical value given by Eq. 4 ($i_{sq,n} = 1.3788$ A). In comparison, the FOC-based control exhibits a higher q-axis current magnitude for the same torque demand. Furthermore, neither strategy employs explicit temperature compensation. However, while the closed-loop PI controllers in standard FOC inherently adjust the applied currents to counteract thermal parameter drifts (such as increasing rotor resistance), the open-loop LUT approach continues to apply setpoints calculated for the nominal, lower temperature. This fundamental difference further contributes to the observed deviations between the two command strategies. Since the LUT-based control relies on nominal motor characteristics and proactively accounts for the active power consumed by iron losses through R_{Fe}, it maintains the expected $i_{s,q}$ level. To maintain the required torque, the LUT-based control accordingly adjusts the current component in the d-axis.

The analysis of the d-axis stator current—which is primarily responsible for establishing the stator flux—reveals more complex behavior. According to Eq. 12, the d-axis stator current is the sum of magnetizing current, i_μ, and d-axis rotor current, $i_{r,d}$. Since the tests are carried out at constant flux (except during the saturation event observed in Fig. 9), the magnetizing current is expected to remain nearly constant. Consequently, variations in the d-axis stator current are largely attributable to changes in d-axis rotor current, which depends on both slip frequency ω_{sl} and the q-axis rotor current, as expressed in Eq. 11.

Because torque and slip always share the same sign, the numerator of Eq. 11 remains positive. Therefore, under constant flux, any torque production – regardless of its sign – should result in an increase of d-axis stator current relative to the no-torque condition. This expected behavior is clearly observed in the LUT-generated d-axis current profiles, where each torque step produces a corresponding rise in d-axis current. In contrast, the FOC-generated d-axis current shows a less pronounced dependence on torque, especially at medium and low speeds. Overall, the LUT-based control systematically yields higher d-axis current levels than the FOC, reflecting its ability to precisely follow the nonlinear magnetization curve rather than relying on a simplified constant inductance.

In the presented experiments, the stator flux was intentionally constrained to emulate specific DC-link voltage limitations. By fixing the flux reference, the optimization algorithm within the LUT generation is restricted and cannot minimize overall losses. Consequently, both control schemes force the induction machine into the exact same physical operating point. The fundamental difference lies in how this point is reached: the LUT method provides precise, model-aware current setpoints directly as a feed-forward action, whereas traditional FOC relies on simplified references that require continuous corrective effort from the closed-loop PI controllers.

The stator current amplitude profiles for nominal and reduced flux operation are presented in Fig. 12. For this specific motor, the maximum stator current is $i_s = 2$ A. Overall, the results obtained with the LUT-based control and FOC show very good agreement under both operating conditions.

Under nominal flux, the LUT-based controller produces currents that are approximately 10–15% higher than those of the FOC at low torque levels. This offset is consistent with the higher d-axis current component observed previously and confirms that the LUTs rely on a larger magnetizing current to establish the desired flux. When moving to reduced flux operation, the discrepancy is significantly reduced, indicating that the observed offset is primarily linked to the flux-producing current.

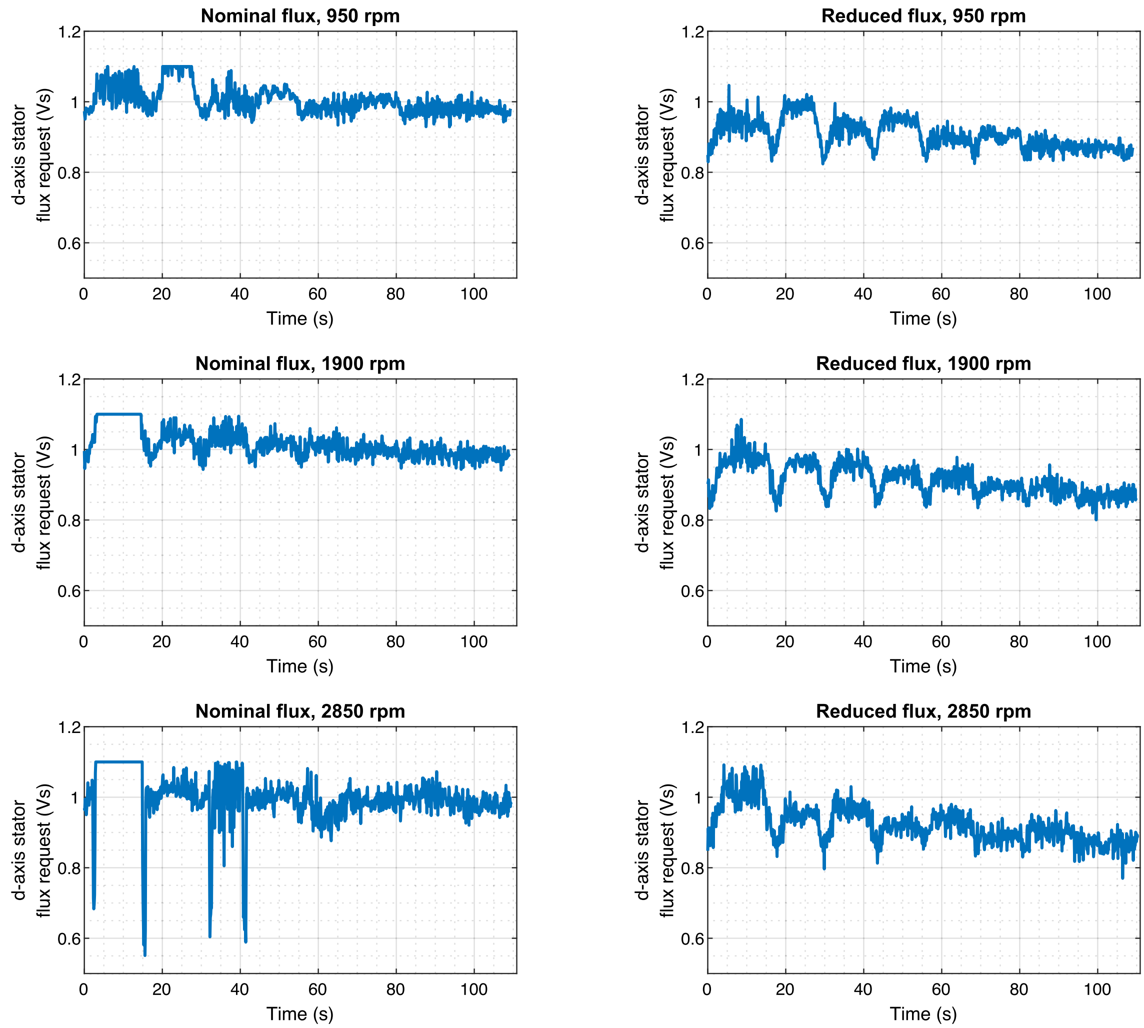

Fig. 9 Requested flux for LUTs

At higher torque levels, the relationship between the two controllers partially inverts, with the FOC currents becoming slightly higher than those of the LUTs. This is likely due to the lower q-axis current demanded by the LUT-based control, which compensates for the effect of its higher d-axis current contribution. As a result, the overall current amplitude profiles closely match across most of the operating points, with differences remaining below 5% during the majority of the steady-state phases and increasing only at low torque values.

A comparison of motor efficiency is presented in Fig. 13. Overall, an excellent agreement is observed between the results obtained with FOC and those from the LUT-based control. For all other operating conditions, efficiency profiles are nearly indistinguishable. A slight advantage for FOC can be seen at low torque levels, particularly under nominal flux operation. This trend is consistent with the observations on stator current amplitude, where the LUT-based controller required slightly higher currents to achieve the same torque at light load. Since copper losses scale with the square of the stator current, this explains the small efficiency gap observed in this operating region.

The accuracy of the LUTs in representing the motor operation from an energetic perspective is further confirmed by Fig. 14, showing the cumulative input energy profiles under both nominal and reduced flux conditions. Differences between FOC and LUTs are small, consistently below 5%. Discrepancies seem to get larger as stator flux is reduced, especially when torque output is small.

4.3 Practical considerations and system boundaries

Although this study focuses on steady-state operation to evaluate energy efficiency, the dynamic behavior of the LUT-based approach should be briefly addressed. While dynamic transients have not been experimentally tested in this work, the LUTs are not expected to introduce any significant control delays. The interpolation process takes only a few microseconds and is executed directly within the fast PWM control

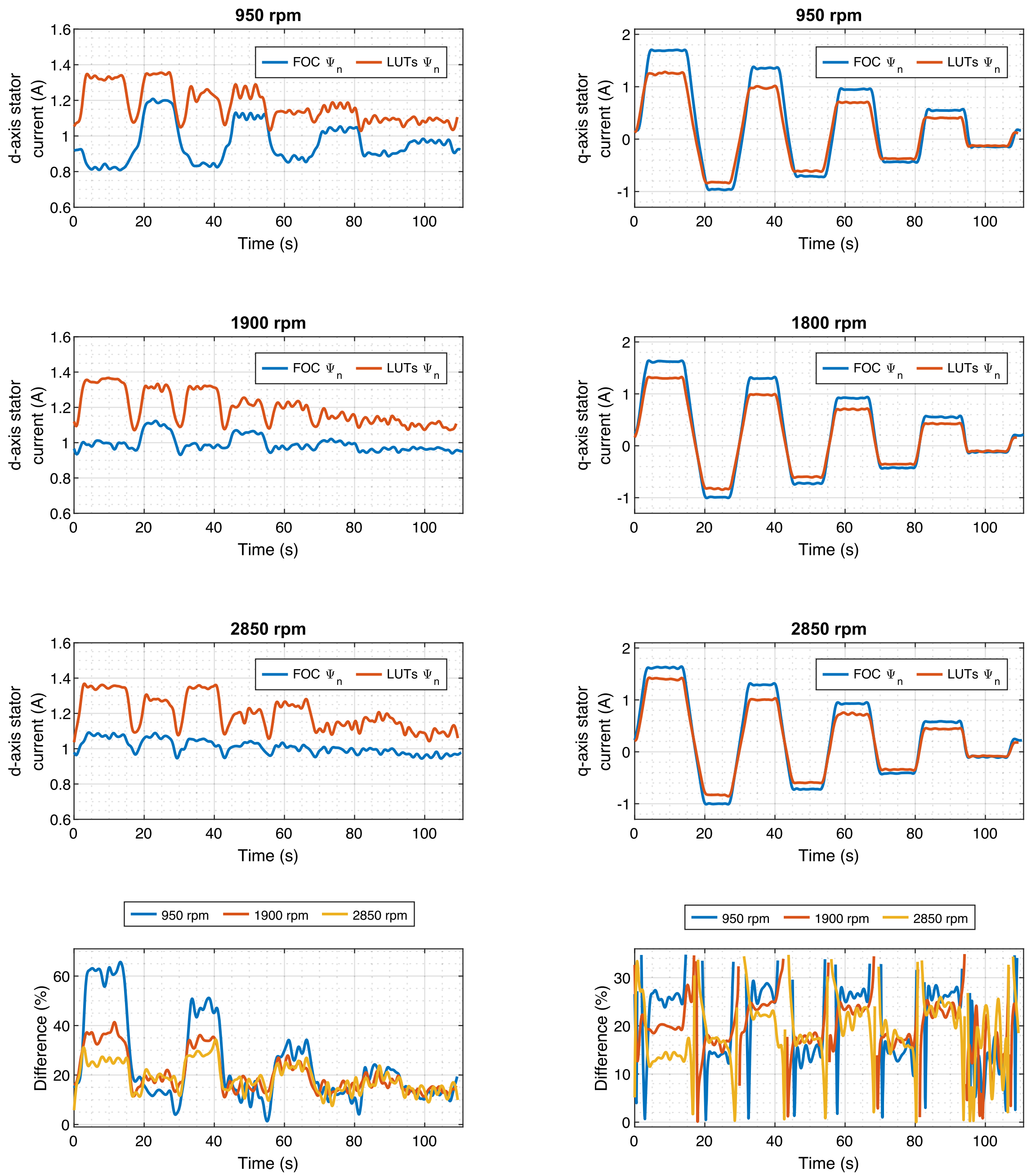

Fig. 10 Measured stator current profiles under nominal flux conditions

loop. In contrast, the speed controller operates in a slower 1 ms loop, and the stator flux dynamics are governed by a much larger electromagnetic time constant. Therefore, the overall dynamic response of the system is determined by the tuning of the PI controllers and the physical limits of the motor, rather than the LUT computation. Additionally, because the LUTs directly provide current setpoints for a given torque request, they essentially act as a feed-forward mechanism, which is expected to support a smooth transient response. Furthermore, in an automotive context, the massive mechanical inertia of a vehicle naturally prevents instantaneous speed changes during regular driving. While all these factors suggest stable and reliable operation, a comprehensive experimental and analytical evaluation of dynamic performance is reserved for future research.

Another practical boundary is the lack of real-time temperature compensation. The presented LUTs are generated for a nominal temperature of 20 °C. However, operational heating alters key machine parameters, such as rotor resistance, which shifts the optimal current trajectories. Because the

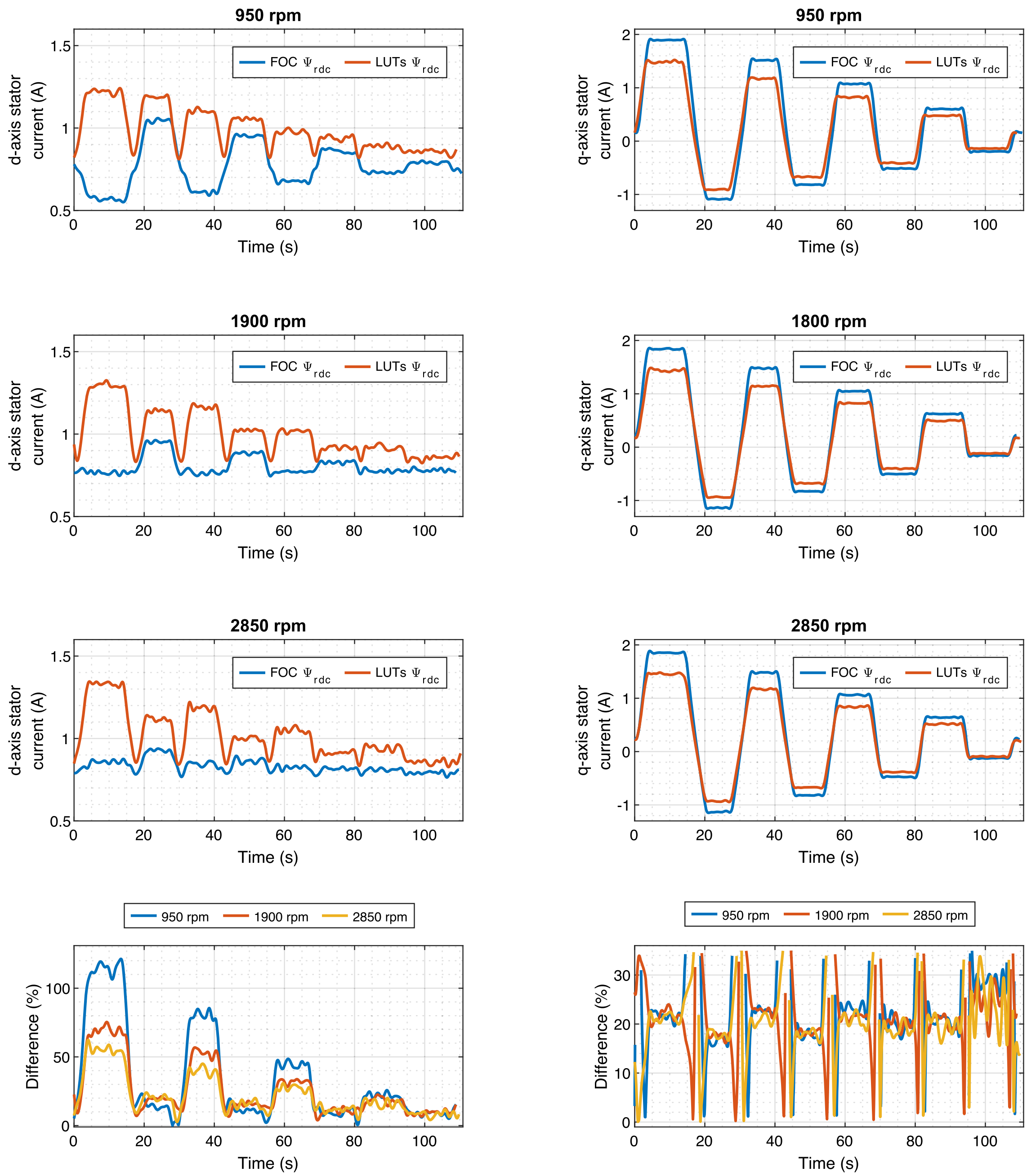

Fig. 11 Measured stator current profiles under reduced flux conditions

LUT approach operates in an open loop, it cannot compensate for these thermal changes. Adding a temperature input would require multidimensional LUTs, significantly increasing data size and computational complexity. This simplification suits early-stage EV simulations, which typically lack detailed thermal models. Ultimately, omitting temperature effects keeps simulations fast while maintaining sufficient accuracy for preliminary energy assessments.

A final practical consideration concerns the physical scale of the experimental setup. The proposed methodology was validated using a small-scale 600-W induction motor, serving primarily as a proof-of-concept case study. Scaling this implementation to full-size automotive traction drives will naturally alter the system's electromagnetic and thermal time constants, as well as the magnitude of nonlinear magnetic effects. However, the fundamental principles of the LUT-based abstraction remain unchanged. Because the specific machine parameters are embedded entirely within the offline LUT generation phase, the proposed architecture is inherently scalable. The core methodology remains fully

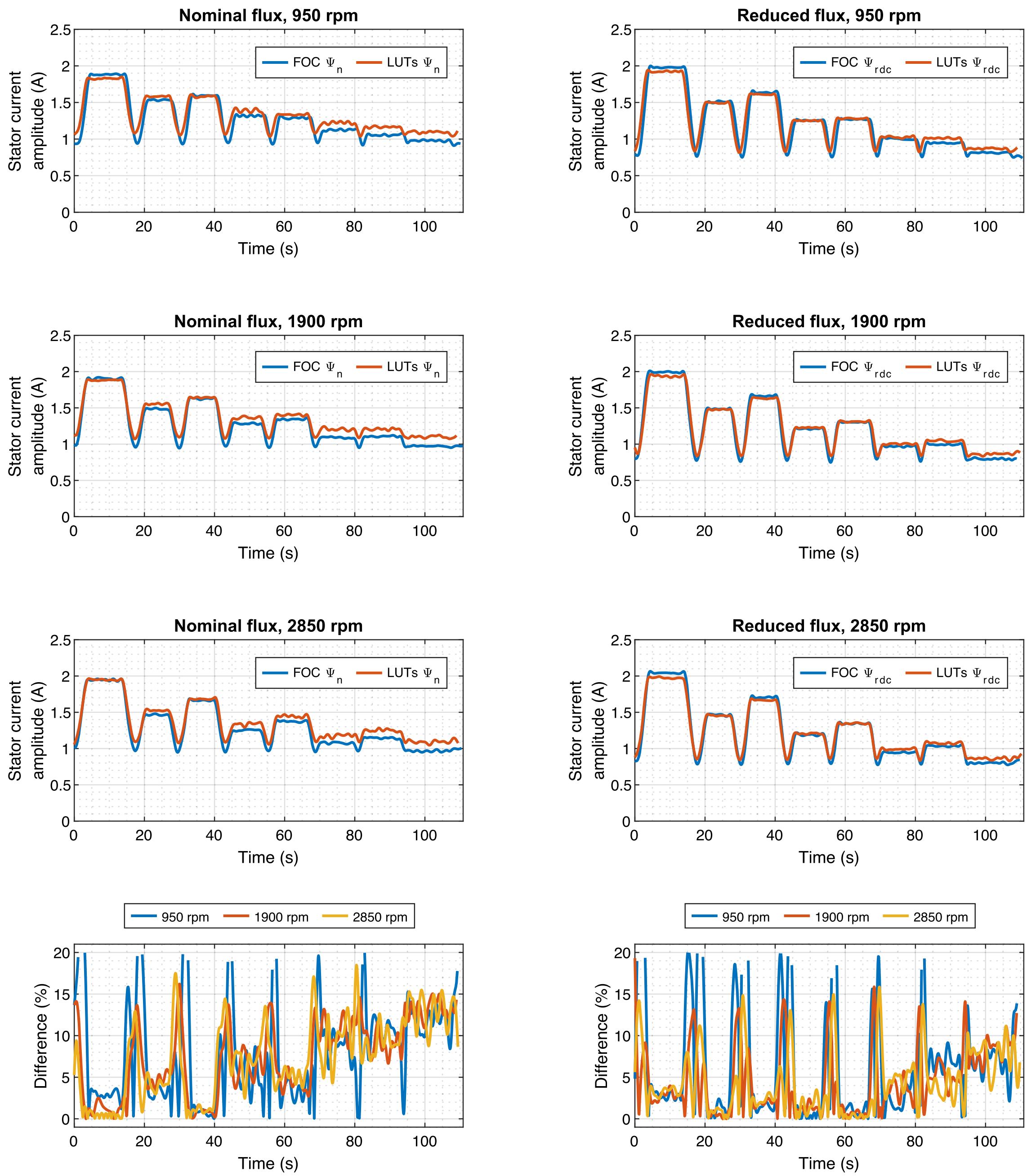

Fig. 12 Measured stator current amplitude profiles

applicable to high-power automotive applications without requiring structural changes to the control abstraction itself.

5 Conclusion

Modeling electric vehicles involves an inherent trade-off between model fidelity and computational efficiency. While energy-based models are fast, they offer a simplified representation. In contrast, high-fidelity equivalent-circuit models are accurate but computationally expensive. This work bridges this gap by experimentally validating the use of LUTs to abstract low-level motor control for system-level powertrain analysis, enabling computationally efficient electric drive simulations.

Applying this methodology to a 600 W induction machine successfully demonstrated its viability as a proof-of-concept for magnet-free powertrain alternatives. Experimental results confirm that the LUT-based abstraction achieves the requested torque and flux targets, maintaining an overall energy con-

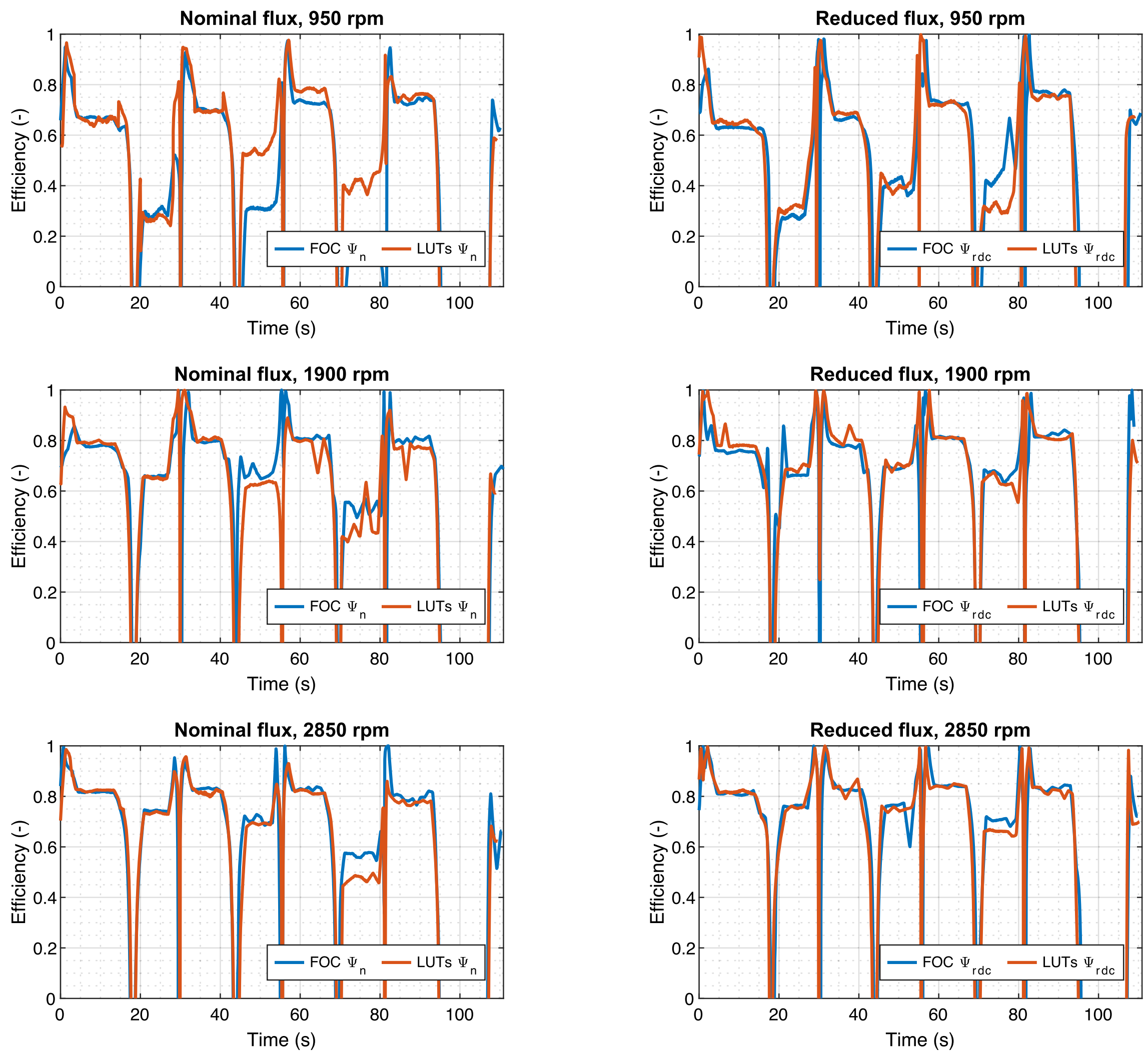

Fig. 13 Measured efficiency profiles

sumption and efficiency equivalent to a traditional FOC scheme. Interestingly, the two control strategies reached the exact same physical operating point through different current trajectories. The LUT-based control commanded systematically higher d-axis and lower q-axis currents. This is a direct result of its detailed underlying model, which proactively accounts for nonlinear magnetic saturation and iron losses, whereas standard FOC relies on a simplified linear representation.

However, the deliberate trade-off prioritizing computational lightness over absolute thermal robustness impacted the stator flux production under high loads. Because the LUTs operate without real-time temperature compensation, they cannot inherently account for thermal parameter drifts, such as increasing rotor resistance. This mismatch ultimately caused the outer flux-control loop to reach the LUT saturation boundary, artificially limiting the d-axis current and resulting in a steady-state flux deviation. While introducing multidimensional, temperature-dependent LUTs could resolve this, it conflicts with the objective of minimizing data requirements and computational overhead.

Despite this practical boundary, the LUT-based method demonstrated strong overall performance and robustness. In conclusion, this research validates that LUTs can effectively abstract motor control behavior without compromising macroscopic energetic accuracy. This makes the proposed framework highly suitable for early-stage EV system studies, where computational speed is critical and detailed thermal data is often unavailable. While this study proves the concept for steady-state operation, future research will investigate its dynamic transient performance.

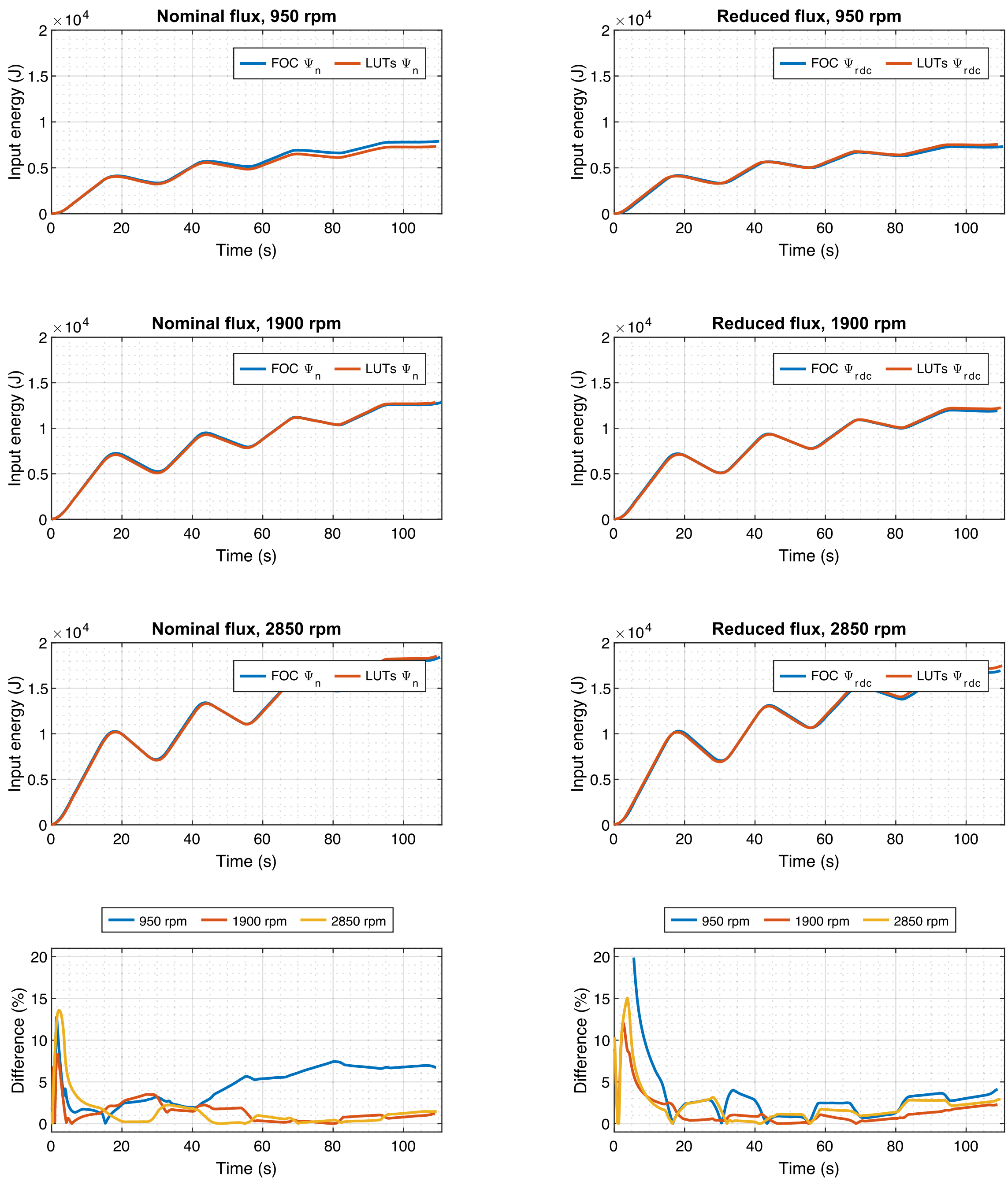

Fig. 14 Measured cumulative input energy profiles

Acknowledgements The research work was carried out in the Centre for Research and Utilization of Renewable Energy (CVVOZE), Brno University of Technology.

Author contributions E.G. and T.L. contributed to validation, visualization, formal analysis, investigation, conceptualization, and methodology. E.G. contributed to software and writing—original draft preparation. M.C. and I.P contributed to resources. T.L. contributed to data curation. E.G., T.L., M.C., and I.P. contributed to writing—review and editing. M.C. and I.P. supervised the study.

Funding Financial support was provided by the Ministry of Education, Youth and Sports of the Czech Republic and the Brno University of Technology under project No. FEKT-S-23-8430.

Data availability No datasets were generated or analyzed during the current study.

Materials Availability Not applicable.

Code availability Not applicable.

Declarations

Conflict of interest The authors declare no conflict of interest.

Ethics approval and consent to participate Not applicable.

Consent for publication All authors have read and agreed to the published version of the manuscript.

References

1. Statista RD (2025) Global market share of electric vehicles within passenger car sales between 2015 and 2023, with a forecast through 2030. https://www.statista.com/statistics/1371599/global-ev-market-share/
2. Dornoff J (2023) Co2 emission standards for new passenger cars and vans in the European union. Int Council Clean Transp
3. Ali A, MacRae C (2024) The evolution of electric vehicle battery technology. https://www.spglobal.com/automotive-insights/en/blogs/2024/11/the-evolution-of-electric-vehicle-battery-technology
4. Carvalho-Pinheiro H (2023) Perfect design tool: electric vehicle modelling and experimental validation. World Electric Veh J. https://doi.org/10.3390/wevj14120337
5. Grano E, Carvalho Pinheiro H, Carello M (2023) A novel electric drive description to bridge the gap between energetic and equivalent-circuit models. Proc Inst Mech Eng Part D J Automob Eng https://doi.org/10.1177/09544070251330340
6. Grano E, Lazek T, Carello M (2024) A numerical methodology for induction motor control: Lookup tables generation and steady-state performance analysis. In: SAE technical paper 2024-01-2152. SAE International https://www.sae.org/publications/technical-papers/content/2024-01-2152/. Accessed 26 May 2025
7. Sabadka D, Molnár V, Fedorko G (2019) Shortening of life cycle and complexity impact on the automotive industry. TEM J 8(4):1295–1301. https://doi.org/10.18421/TEM84-27
8. Rizzoni G, Guzzella L, Baumann BM (1999) Unified modeling of hybrid electric vehicle drivetrains. IEEE/ASME Trans Mechatron 4(3):246–257. https://doi.org/10.1109/3516.789683
9. Guzzella L, Sciarretta A (2007) Electric and hybrid-electric propulsion systems. Springer, Berlin https://doi.org/10.1007/978-3-540-74692-8_4
10. Sciarretta A, Nunzio G, Leon Ojeda L (2015) Optimal ecodriving control: energy-efficient driving of road vehicles as an optimal control problem. IEEE Control Syst Mag 35(5):71–90. https://doi.org/10.1109/MCS.2015.2449688
11. Ponso A, Bonfitto A, Belingardi G (2023) Route planning for electric vehicles including driving style, HVAC, payload and battery health. Energies https://doi.org/10.3390/en16124627
12. Kim N, Cha SW, Peng H (2012) Optimal equivalent fuel consumption for hybrid electric vehicles. IEEE Trans Control Syst Technol 20(3):817–825. https://doi.org/10.1109/TCST.2011.2123099
13. Plett G (2015) Battery management systems. In: Battery Modeling, vol I
14. Pukrushpan JT, Peng H, Stefanopoulou AG (2004) Control-oriented modeling and analysis for automotive fuel cell systems. J Dyn Syst Meas Contr 126(1):14–25. https://doi.org/10.1115/1.1648308
15. Pellegrino G, Bojoi RI, Guglielmi P (2011) Unified direct-flux vector control for AC motor drives. IEEE Trans Ind Appl 47(5):2093–2102. https://doi.org/10.1109/TIA.2011.2161532
16. Trzynadlowski AM (2001) Control of induction motors. Academic Press, San Diego. https://doi.org/10.1016/B978-012701510-1/50010-6
17. Quang NP, Dittrich J-A (2015) Vector control of three-phase AC machines, 2nd edn. Springer, Berlin https://doi.org/10.1007/978-3-662-46915-6
18. Grano E, Bianco E, De Carvalho Pinheiro H, Carello M (2023) MTPA and flux weakening control of electric motors: a numerical approach. In: 2023 IEEE international conference on environment and electrical engineering and 2023 IEEE industrial and commercial power systems Europe (EEEIC/I&CPS Europe), pp 1–7. https://doi.org/10.1109/EEEIC/ICPSEurope57605.2023.10194684
19. Toman M, Cipin R, Vorel P, Mach M (2018) Algorithm for IM optimal flux determination respecting nonlinearities and thermal influences. In: 2018 IEEE international conference on environment and electrical engineering and 2018 IEEE industrial and commercial power systems Europe (EEEIC / I&CPS Europe), pp 1–5 https://doi.org/10.1109/EEEIC.2018.8493953
20. Rubino S, Tolosano L, Mandrile F, Armando E, Bojoi R (2023) Flux polar control (FPC): a unified torque controller for AC motor drives. IEEE Trans Ind Appl 59(4):4140–4163. https://doi.org/10.1109/TIA.2023.3270110
21. Inoue Y, Morimoto S, Sanada M (2011) Comparative study of PMSM drive systems based on current control and direct torque control in flux-weakening control region. In: 2011 IEEE international electric machines & drives conference (IEMDC), pp 1094–1099. https://doi.org/10.1109/IEMDC.2011.5994754
22. Grano E, Carello M (2025) Hardware-oriented LUT generation algorithm for d–q axis stator current reference in electric drive systems. In: 2025 IEEE international conference on environment and electrical engineering and 2025 IEEE industrial and commercial power systems Europe (EEEIC/I&CPS Europe), pp 1–6. https://doi.org/10.1109/EEEIC/ICPSEurope64998.2025.11169124
23. LCM: X2C: Model-based development and code generation of real time control for microprocessors. Developed by LCM—the mechatronic engineering company. https://x2c.lcm.at/